Wavefront Coding Fluorescence Microscopy Using High Aperture Lenses

Matthew R. Arnison*, Carol J. Cogswell†, Colin J. R. Sheppard*, Peter Török‡

* University of Sydney, Australia
† University of Colorado, U. S. A.
‡ Imperial College, U. K.

1 Extended Depth of Field Microscopy

In recent years live cell fluorescence microscopy has become increasingly important in biological and medical studies. This is largely due to new genetic engineering techniques which allow cell features to grow their own fluorescent markers. A popular example is green fluorescent protein. This avoids the need to stain, and thereby kill, a cell specimen before taking fluorescence images, and thus provides a major new method for observing live cell dynamics.

With this new opportunity come new challenges. Because in earlier days the process of staining killed the cells, microscopists could do little additional harm by squashing the preparation to make it flat, thereby making it easier to image with a high resolution, shallow depth of field lens. In modern live cell fluorescence imaging, the specimen may be quite thick (in optical terms). Yet a single 2D image per time–step may still be sufficient for many studies, as long as there is a large depth of field as well as high resolution.

Light is a scarce resource for live cell fluorescence microscopy. To image rapidly changing specimens the microscopist needs to capture images quickly. One of the chief constraints on imaging speed is the light intensity. Increasing the illumination will result in faster acquisition, but can affect specimen behaviour through heating, or reduce fluorescent intensity through photobleaching.

Another major constraint is the depth of field. Working at high resolution gives a very thin plane of focus, leading to the need to constantly "hunt" with the focus knob while viewing thick specimens with rapidly moving or changing features. When recording data, such situations require the time-consuming capture of multiple focal planes, thus making it nearly impossible to perform many live cell studies.

Ideally we would like to achieve the following goals:

- use all available light to acquire images quickly,
- achieve maximum lateral resolution,
- and yet have a large depth of field.

However, such goals are contradictory in a normal microscope.

For a high aperture aplanatic lens, the depth of field is [18]

$$\Delta z = 1.77\lambda / \left[4 \sin^2 \frac{\alpha}{2} \left(1 - \frac{1}{3} \tan^4 \frac{\alpha}{2} \right) \right] , \tag{1}$$

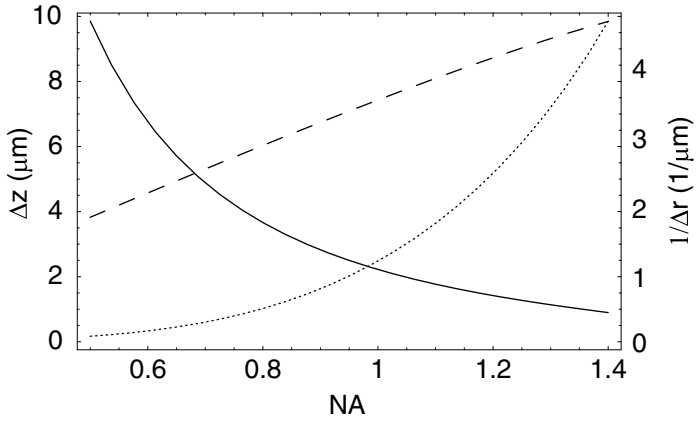

Figure1. Depth of field (*solid line*), lateral resolution (*dashed line*) and peak intensity at focus (*dotted line* – arbitrary units) for an oil immersion ($n_{\text{oil}} = 1.518$) aplanatic microscope objective with a typical range of NA and $\lambda_0 = 0.53\,\mu\text{m}$ is the vacuum wavelength

where Δz is defined as the distance along the optical axis for which the intensity is more than half the maximum. Here the focal region wavelength is λ and the aperture half–angle is α. A high aperture value for the lateral resolution can be approximated from the full–width at half–maximum (FWHM) of the unpolarised intensity point spread function (PSF) [17]. We can use the same PSF to find the peak intensity at focus, as a rough indication of the high aperture light collection efficiency,

$$I_{\text{focus}} \propto \left[1 - \frac{5}{8}(\cos^{\frac{3}{2}}\alpha)(1 + \frac{3}{5}\cos\alpha)\right]^2 . \tag{2}$$

These relationships are plotted in Fig. 1 for a range of numerical apertures (NA),

$$\text{NA} = n_1 \sin\alpha \tag{3}$$

where n_1 is the refractive index of the immersion medium. Clearly maximising the depth of field conflicts with the goals of high resolution and light efficiency.

1.1 Methods For Extending the Depth of Field

A number of methods have been proposed to work around these limitations and produce an extended depth of field (EDF) microscope.

Before the advent of charge–coupled device (CCD) cameras, Häusler [8] proposed a two step method to extend the depth of focus for incoherent microscopy. First, an axially integrated photographic image is acquired by leaving the camera shutter open while the focus is smoothly changed. The second step is to deconvolve the image with the integration system transfer function. Häusler showed that as long as the focus change is more than twice the thickness of the object, the transfer function does not change for parts of the object at different depths — effectively the

transfer function is invariant with defocus. The transfer function also has no zeros, providing for easy single–step deconvolution.

This method could be performed easily with a modern microscope, as demonstrated recently by Juškaitis *et al* [11]. However, the need to smoothly vary the focus is a time–consuming task requiring some sort of optical displacement within the microscope. This is in conflict with our goal of rapid image acquisition.

A similar approach is to simply image each plane of the specimen, stepping through focus, then construct an EDF image by taking the axial average of the 3D image stack, or some other more sophisticated operation which selects the best focused pixel for each transverse specimen point. This has been described in application to confocal microscopy [21], where the optical sectioning makes the EDF post–processing straightforward. Widefield deconvolution images could also be used. In both cases the focal scanning and multiple plane image capture are major limitations on overall acquisition speed.

Potuluri *et al* [16] have demonstrated the use of rotational shear interferometry with a conventional widefield transmission microscope. This technique, using incoherent light, adds significant complexity, and sacrifices some signal–to–noise ratio (SNR). However the authors claim an effectively infinite depth of field. The main practical limit on the depth of field is the change in magnification with depth (perspective projection) and the rapid drop in image contrast away from the imaging lens focal plane.

Another approach is to use a pupil mask to increase the depth of field, combined with digital image restoration. This creates a digital–optical microscope system. Designing with such a combination in mind allows additional capabilities not possible with a purely optical system. We can think of the pupil as encoding the optical wavefront, so that digital restoration can decode a final image, which gives us the term *wavefront coding*.

In general a pupil mask will be some complex function of amplitude and phase. The function might be smoothly varying, and therefore usable over a range of wavelengths. Or it might be discontinuous in step sizes that depend on the wavelength, such as a binary phase mask.

Many articles have explored the use of amplitude pupil masks [14,15,25], including for high aperture systems [4]. These can be effective at increasing the depth of field, but they do tend to reduce dramatically the light throughput of the pupil. This poses a major problem for low light fluorescence microscopy.

Wilson *et al* [26] have designed a system which combines an annulus with a binary phase mask. The phase mask places most of the input beam power into the transmitting part of the annular pupil, which gives a large boost in light throughput compared to using the annulus alone. This combination gives a ten times increase in depth of field. The EDF image is laterally scanned in x and y, and then deconvolution is applied as a post–processing step.

Binary phase masks are popular in lithography where the wavelength can be fixed. However, in widefield microscopy any optical component that depends on a certain wavelength imposes serious restrictions. In epi-fluorescence, the incident

and excited light both pass through the same lens. Since the incident and excited light are at different wavelengths, any wavelength dependent pupil masks would need to be imaged onto the lens pupil from beyond the beam splitter that separates the incoming and outgoing light paths. This adds significant complexity to the optical design of a widefield microscope.

The system proposed by Wilson *et al* [26] is designed for two-photon confocal microscopy. Optical complexity, monochromatic light, and scanning are issues that confocal microscopy needs to deal with anyway, so this method of PSF engineering adds relatively little overhead.

Wavefront coding is an incoherent imaging technique that relies on the use of a smoothly varying phase–only pupil mask, along with digital processing. Two specific functions that have been successful are the cubic [3,6] and logarithmic [5] phase masks, where the phase is a cubic or logarithmic function of distance from the centre of the pupil, in either radial or rectangular co-ordinates. The logarithmic design is investigated in detail in Chap. **??**.

The cubic phase mask (CPM) was part of the first generation wavefront coding systems, designed for general EDF imaging. The CPM has since been investigated for use in standard (low aperture) microscopy [24]. The mask can give a ten times increase in the depth of field without loss of transverse resolution.

Converting a standard widefield microscope to a wavefront coding system is straightforward. The phase mask is simply placed in the back pupil of the microscope objective. The digital restoration is a simple single-step deconvolution, which can operate at video rates. Once a phase mask is chosen to match a lens and application, an appropriate digital inverse filter can be designed by measuring the PSF. The resulting optical–digital system is specimen independent.

The main trade off is a lowering of the SNR as compared with normal widefield imaging. The CPM also introduces an imaging artefact where specimen features away from best focus are slightly laterally shifted in the image. This is in addition to a perspective projection due to the imaging geometry, since an EDF image is obtained from a lens at a single position on the optical axis. Finally, as the CPM is a rectangular design, it strongly emphasises spatial frequencies that are aligned with the CCD pixel axes.

High aperture imaging does produce the best lateral resolution, but it also requires more complex theory to model accurately. Yet nearly all of the investigations of EDF techniques reviewed above are low aperture. In this chapter we choose a particular EDF method, wavefront coding with a cubic phase plate, and investigate its experimental and theoretical performance for high aperture microscopy.

2 High Aperture Fluorescence Microscopy Imaging

A wavefront coding microscope is a relatively simple modification of a modern microscope. A system overview is shown in Fig. 2.

The key optical element in a wavefront coding system is the waveplate. This is a transparent molded plastic disc with a precise aspheric height variation. Placing the

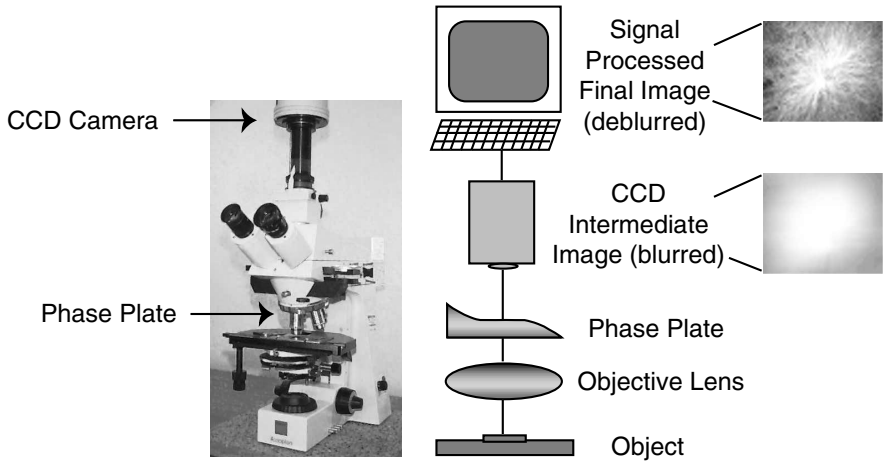

Figure2. An overview of a wavefront coding microscope system. The image-forming light from the object passes through the objective lens and phase plate and produces an intermediate encoded image on the CCD camera. This blurred image is then digitally filtered (decoded) to produce the extended depth of field result. Examples at right show the fluorescing cell image of Fig. 7(c) at each stage of the two–step process. At lower left an arrow shows where the phase plate is inserted into the microscope

waveplate in the back focal plane of a lens introduces a phase aberration designed to create invariance in the optical system against some chosen imaging parameter. A cubic phase function on the waveplate is useful for microscopy, as it makes the low aperture optical transfer function (OTF) insensitive to defocus.

While the optical image produced is quite blurry, it is uniformly blurred over a large range along the optical axis through the specimen (Fig. 3). From this blurred intermediate image, we can digitally reconstruct a sharp EDF image, using a measured PSF of the system and a single step deconvolution. The waveplate and digital filter are chosen to match a particular objective lens and imaging mode, with the digital filter further calibrated by the measured PSF. Once these steps are carried out, wavefront coding works well for any typical specimen.

The EDF behaviour relies on modifying the light collection optics only, which is why it can be used in other imaging systems such as photographic cameras, without needing precise control over the illumination light. In epi-fluorescence both the illumination light and the fluorescent light pass through the waveplate. The CPM provides a beneficial effect on the illumination side, by spreading out the axial range of stimulation in the specimen, which will improve the SNR for planes away from best focus.

2.1 Experimental Method

The experimental setup followed the system outline shown in Fig. 2. We used a Zeiss Axioplan microscope with a Plan Neofluar 40x 1.3 NA oil immersion objective. The

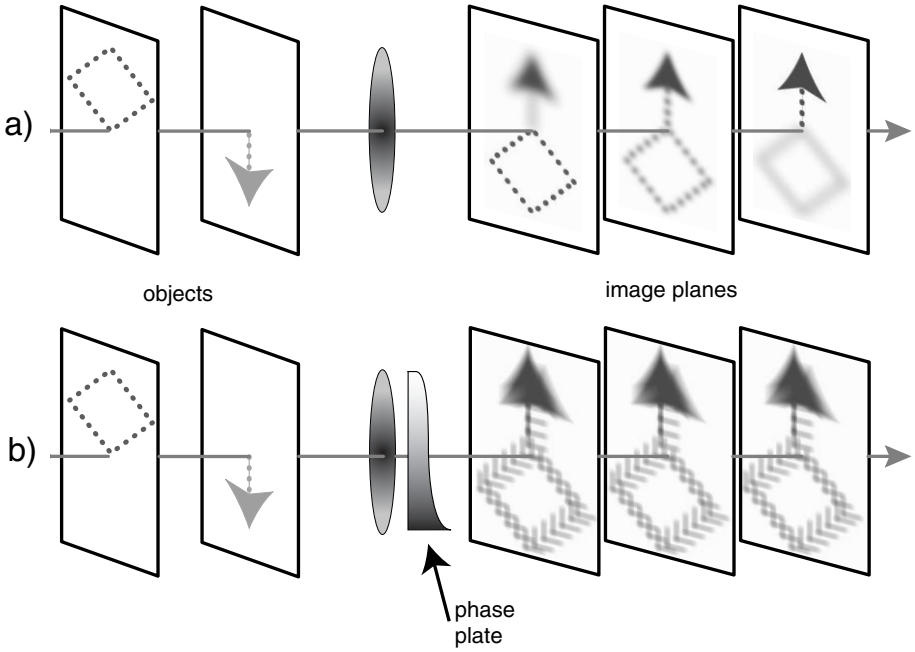

Figure3. How points are imaged in standard versus wavefront coding systems: (**a**) Conventional (small depth of field) system with two axially–separated objects to the left of a lens. Because each object obtains best focus at a different image plane, the arrow object points decrease in diameter toward their plane of best focus (far right), while the object points of the diamond are increasingly blurred. (**b**) Inserting a CPM phase plate causes points from both objects to be equivalently blurred over the same range of image planes. Signal processing can be applied to any one of these images to remove the constant blur and produce a sharply–focused EDF image

wavefront coding plate was a rectangular cubic phase function design (CPM 127-R60 Phase Mask from CDM Optics, Boulder, CO, USA) with a peak to valley phase change of 56.6 waves at 546 nm across a 13 mm diameter optical surface. This plate was placed in a custom mount and inserted into the differential interference contrast slider slot immediately above the objective, and aligned so that it was centred with the optical axis, covering the back pupil.

A custom square aperture mask was inserted into an auxiliary slot 22 mm above the lens, with the square mask cut to fit inside the 10 mm circular pupil of the objective lens. This square mask is needed due to the rectangular nature of the CPM function,

$$\varphi(m,n) = A(m^3 + n^3)\,, \tag{4}$$

where m and n are the Cartesian co-ordinates across the pupil and A is the strength of the phase mask (see Fig. 4). The square mask was rotated to match the mn axes of

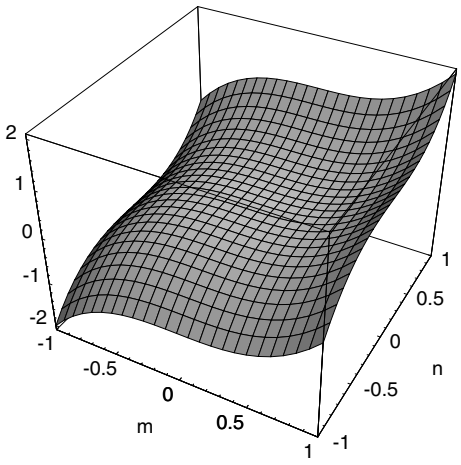

Figure4. Height variation across the cubic phase mask given in (4), for $A = 1$

the CPM. For comparison, standard widefield fluorescence imaging was performed without the CPM or the square aperture mask in place.

Images were taken in epi-fluorescence mode with a mercury lamp (HBO 50 W) and fluorescein isothiocyanate (FITC) fluorescence filters in place. Images were recorded with a Photometrics cooled camera (CH250) with a Thomson TH 7895 CCD at 12 bit precision. To ensure we were sampling at the maximum resolution of the 1.3 NA lens, a 2.5x eyepiece was inserted just before the camera inside a custom camera mount tube. This tube also allowed precise rotational alignment of the camera, in order to match the CCD pixel array *xy* axes with the CPM *mn* axes.

With 100x total magnification and 19 μm square CCD pixels, this setup gave a resolution of 0.19 μm per pixel. This is just below the theoretical maximum resolution of 0.22 μm for a 1.3 NA lens (see Fig. 1), for which critical sampling would be 0.11 μm per pixel, so the results are slightly under sampled.

The PSF was measured using a 1 μm diameter polystyrene bead stained with FITC dye. The peak emission wavelength for FITC is 530 nm. Two dimensional PSF images were taken over a focal range of 10 μm in 1 μm steps. This PSF measurement was used to design an inverse filter to restore the EDF image. The OTF was obtained from the Fourier transform of the 2D PSF.

Each wavefront coding intermediate image was a single exposure on the CCD camera. A least squares filter was incorporated into the inverse filter to suppress noise beyond the spatial frequency cutoff of the optical system. A final wavefront coding image was obtained by applying the inverse filter to a single intermediate image.

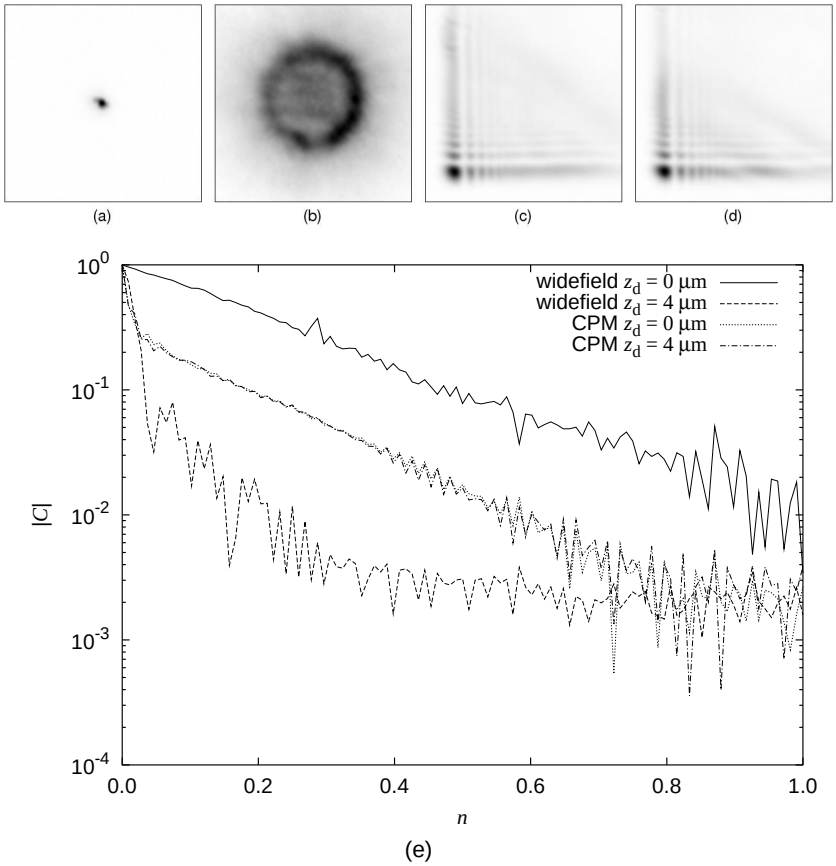

Figure5. Experimental PSFs and OTFs for the widefield and wavefront coding systems as measured using a 1 µm fluorescent bead and a NA = 1.3 oil objective.For each type of microscope, a PSF from the plane of best focus is followed by one with 4 µm defocus. The upper images (a-d) show the intensity of a central region of the PSF whilst the lower graph (e) gives the magnitude of the OTF for a line $m = 0$ through the OTF for each case: (**a**) widefield $z_d = 0$ µm (*solid line*), (**b**) widefield defocused $z_d = 4$ µm (*dashed line*), (**c**) CPM $z_d = 0$ µm (*dotted line*), (**d**) CPM defocused $z_d = 4$ µm (*dash–dotted line*). The spatial frequency n has been been normalised so that $n = 1$ lies at the CCD camera spatial frequency cutoff. The PSFs have area 13 µm × 13 µm

2.2 PSF and OTF Results

The measured PSFs and derived OTFs for the focused and 4 µm defocused cases are shown in Fig. 5, comparing standard widefield microscopy with wavefront coding using a CPM.

The widefield PSF shows dramatic change with defocus as expected for a high aperture image of a 1 µm bead. But the wavefront coding PSF shows very little change after being defocused by the same amount.

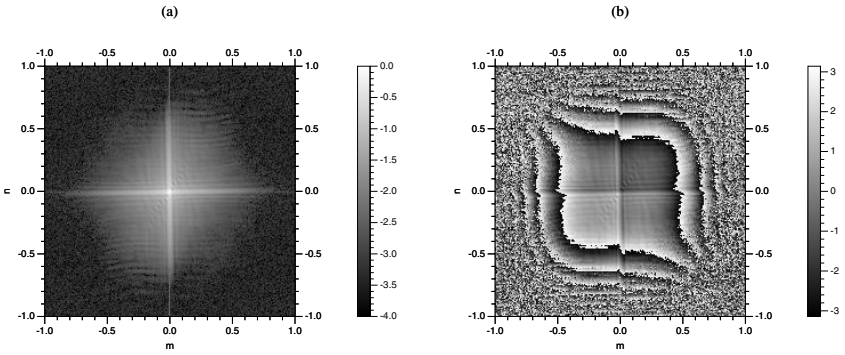

Figure6. The measured CPM in–focus 2D OTF: (**a**) is the magnitude of the OTF in $\log_{10}$ scale, and (**b**) is the wrapped OTF phase in radians. The spatial frequencies m and n have been been normalised so that $|m|, |n| = 1$ lies at the CCD camera spatial frequency cutoff

The OTF measurements emphasise this focus independence for the wavefront coding system. While the in–focus OTF for the widefield system has the best overall response, the OTF quickly drops after defocusing. The widefield defocused OTF also has many nulls before the spatial frequency cutoff, indicated in these results by a downward spike. These nulls make it impossible in widefield to use the most straightforward method of deconvolution – division of the image by the system OTF in Fourier space. Time consuming iterative solutions must be used instead.

The wavefront coding system OTF shows a reduced SNR compared with the in–focus widefield OTF. Yet the same SNR is maintained through a wide change in focus, indicating a depth of field at least 8 times higher than the widefield system. The CPM frequency response extends to 80% of the spatial frequency cutoff of the widefield case before descending into the noise floor. This indicates that the wavefront coding system has maintained much of the transverse resolution expected from the high aperture lens used. Because there are no nulls in the CPM OTF at spatial frequencies below the SNR imposed cutoff, deconvolution can be performed using a single–pass inverse filter based on the reciprocal of the system OTF.

A limiting factor on the SNR, and therefore the wavefront coding system resolution, is the CCD camera dynamic range of 12 bits, giving a noise floor of at least 2.4×10^{-4}. From Fig. 5(e) the effective noise floor seems to be a bit higher at 10^{-3}. This has a greater impact on the off–axis spatial frequencies, where a higher SNR is required to maintain high spatial frequency response, an effect which is clearly seen in the measured 2D OTF in Fig. 6.

2.3 Biological Imaging Results

In order to experimentally test high resolution biological imaging using the CPM wavefront coding system in epi-fluorescence, we imaged an anti-tubulin / FITC–labeled HeLa cell. For comparison, we also imaged the same mitotic nucleus in both a standard widefield fluorescence microscope and a confocal laser scanning

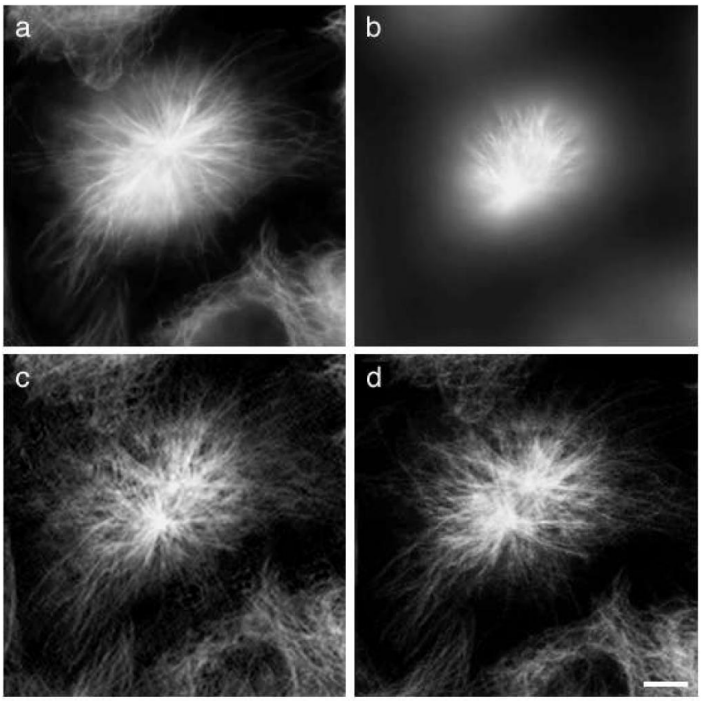

Figure7. Comparison images of an antitubulin / FITC–labeled HeLa cell nucleus obtained using three kinds of microscope. (**a**-**b**) Conventional widefield fluorescence images of the same mitotic nucleus acquired at two different focal planes, 6 µm apart in depth. Misfocus blurring is prevalent, with only one of the two centrioles in focus in each image. (**c**) A CPM wavefront coding image of this nucleus greatly increases focal depth so that now both centrioles in the mitotic spindle are sharply focused. (**d**) An equivalent confocal fluorescence EDF image obtained by averaging 24 separate planes of focus, spaced 0.5 µm apart. The resolutions of the wavefront coding and confocal images are comparable but the confocal image took over 20 times longer to produce. Note that wavefront coding gives a perspective projection and confocal gives an isometric projection, which chiefly accounts for their slight difference in appearance.Objective NA=1.3 oil, scale bar: 6 µm

system (Fig. 7). The first widefield image, Fig. 7(a), shows a mitotic nucleus with one centriole in sharp focus, while a second centriole higher in the specimen is blurred. This feature became sharp when the focus was altered by 6 µm, as shown in Fig. 7(b). The wavefront coding system image in Fig. 7(c) shows a much greater depth of field, with both centrioles in focus in the same image. We observed a depth of field increase of at least 6 times compared with the widefield system, giving a 6 µm depth of field for the wavefront coding system for the NA = 1.3 oil objective.

For further comparison, we imaged the same specimen using a confocal microscope. A simulated EDF image is shown in Fig. 7(d), obtained by averaging 24 planes of focus. This gives an image of similar quality to the wavefront coding im-

age. However, the confocal system took over 20 times longer to acquire the data for this image, due to the need to scan the image point in all three dimensions. There is also a change in projection geometry between the two systems. The confocal EDF image has orthogonal projection, whereas the wavefront coding EDF image has perspective projection.

3 Wavefront Coding Theory

In this section we will investigate theoretical models for wavefront coding microscopy. We present a summary of the development of the cubic phase function and the paraxial theory initially used to model it. We then analyse the system using vectorial high aperture theory, as is normally required for accuracy with a 1.3 NA lens.

High aperture vectorial models of the PSF for a fluorescence microscope are well developed [9,23]. The Fourier space equivalent, the OTF, also has a long history [7,13,20]. However, the CPM defined in (4) is an unusual microscope element:

1. Microscope optics usually have radial symmetry around the optical axis, which the CPM does not.
2. The CPM gives a very large phase aberration of up to 60 waves, whilst most aberration models are oriented towards phase strengths on the order of a wave at most.
3. In addition, the CPM spreads the light over a very long focal range, whilst most PSF calculations can assume the energy drops off very rapidly away from focus.

These peculiarities have meant we needed to take particular care with numerical computation in order to ensure accuracy, and in the case of the OTF modeling the radial asymmetry has motivated a reformulation of previous symmetric OTF theory.

3.1 Derivation of the Cubic Phase Function

There are various methods that may be used to derive a pupil phase function which has the desired characteristics for EDF imaging. The general form of a phase function in Cartesian co-ordinates is

$$T(m,n) = \exp[\mathrm{i}k\varphi(m,n)] \,, \tag{5}$$

where m, n are the lateral pupil co-ordinates and $k = 2\pi/\lambda$ is the wave-number. The cubic phase function was found by Dowski and Cathey [6] using paraxial optics theory by assuming the desired phase function is a simple 1D function of the form

$$\varphi(m) = Am^{\gamma}, \ \gamma \neq \{0,1\}, \ A \neq 0 \,. \tag{6}$$

By searching for the values of A and γ which give an OTF which does not change through focus, they found, using the stationary phase approximation and the ambiguity function, that the best solution was for $A \gg 20/k$ and $\gamma = 3$. Multiplying out to 2D, this gives the cubic phase function in (4).

3.2 Paraxial Model

Using the Fraunhofer approximation, as suitable for low NA, we can write down a 1D pupil transmission function encompassing the effects of cubic phase (4) and defocus,

$$T(m) = \exp[\mathrm{i}k\varphi(m)] \exp(\mathrm{i}m^2\psi) \,, \tag{7}$$

where ψ is a defocus parameter. We then find the 1D PSF is

$$E(x) = \int_{-1}^{1} T(m) \exp(\mathrm{i}xm)\mathrm{d}m \,, \tag{8}$$

where x is the lateral co-ordinate in the PSF . The 1D OTF is

$$C(m) = \int_{-1}^{1} T(m' + m/2)\mathrm{T}^*(m' - m/2)\mathrm{d}m' \,. \tag{9}$$

The 2D PSF is simply $E(x)E(y)$.

Naturally this 1D CPM gives behaviour in which, in low aperture systems at least, the lateral x and y imaging axes are independent of each other. This gives significant speed boosts in digital post–processing. Another important property of the CPM is that the OTF does not reach zero below the spatial frequency cutoff which means that deconvolution can be carried out in a single step. The lengthy iterative processing of widefield deconvolution is largely due to the many zeros in the conventional defocused OTF. Another important feature of Fraunhofer optics is that PSF changes with defocus are limited to scaling changes. Structural changes in the PSF pattern are not possible.

This paraxial model for the cubic phase mask has been thoroughly verified experimentally for low NA systems [3,24].

3.3 High Aperture PSF Model

We now explore the theoretical behaviour for a high NA cubic phase system. Normally we need high aperture theory for accurate modeling of lenses with NA > 0.5. However large aberrations like our cubic phase mask can sometimes overwhelm the high NA aspects of focusing. By comparing the paraxial and high NA model results we can determine the accuracy of the paraxial approximation for particular wavefront coding systems.

The theory of Richards and Wolf [17] describes how to determine the electric field near to the focus of a lens which is illuminated by a plane polarised quasi-monochromatic light wave. Their analysis assumes very large values of the Fresnel number, equivalent to the Debye approximation. We can then write the equation for the vectorial amplitude PSF $\boldsymbol{E}(\boldsymbol{x})$ of a high NA lens illuminated with a plane polarised wave as the Fourier transform of the complex vectorial pupil function $\boldsymbol{Q}(\boldsymbol{m})$ [13],

$$\boldsymbol{E}(\boldsymbol{x}) = -\frac{ik}{2\pi} \int\int\int \boldsymbol{Q}(\boldsymbol{m}) \exp(\mathrm{i}k\boldsymbol{m} \cdot \boldsymbol{x})\mathrm{d}\boldsymbol{m} \,. \tag{10}$$

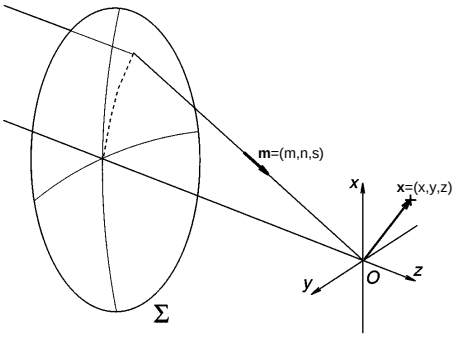

Figure8. Diagram of the light focusing geometry used in calculating the high NA PSF, indicating the focal region co-ordinate $\boldsymbol{x}$ and the pupil co-ordinate $\boldsymbol{m}$, the latter of which may also be thought of as a unit vector aligned with a ray from the pupil to the focal point O

Here $\boldsymbol{m} = (m, n, s)$ is the Cartesian pupil co-ordinate, and $\boldsymbol{x} = (x, y, z)$ is the focal region co-ordinate. The z axis is aligned with the optical axis, and s is the corresponding pupil co-ordinate, as shown in Fig. 8. The vectorial pupil function $\boldsymbol{Q}(\boldsymbol{m})$ describes the effect of a lens on the polarisation of the incident field, the complex value of any amplitude or phase filters across the aperture, and any additional aberration in the lens focusing behaviour from that which produces a perfect spherical wavefront converging on the focal point.

From the Helmholtz equation for a homogeneous medium, assuming constant refractive index in the focal region, we know that the pupil function is only non-zero on the surface of a sphere with radius k,

$$\boldsymbol{Q}(\boldsymbol{m}) = \boldsymbol{P}(\boldsymbol{m})\delta(|\boldsymbol{m}| - k^2) \; . \tag{11}$$

Because the pupil function only exists on the surface of a sphere, we can slice it along the $s = 0$ plane into a pair of functions

$$\boldsymbol{Q}(\boldsymbol{m}) = \boldsymbol{Q}(\boldsymbol{m})\frac{k}{s}\delta(s - \sqrt{k^2 - l^2}) + \boldsymbol{Q}(\boldsymbol{m})\frac{k}{s}\delta(s + \sqrt{k^2 - l^2}) \; , \tag{12}$$

representing forward and backward propagation [1,22]. Here we have introduced a radial co-ordinate $l = \sqrt{m^2 + n^2}$. Now we take the axial projection $\boldsymbol{P}_+(m, n)$ of the forward propagating component of the pupil function,

$$\boldsymbol{P}_+(m, n) = \int_0^\infty \boldsymbol{Q}(\boldsymbol{m})\frac{k}{s}\delta(s - \sqrt{k^2 - l^2})\mathrm{d}s \tag{13}$$

$$= \boldsymbol{Q}(m, n, s_+)\frac{1}{s_+} \; , \tag{14}$$

where we have normalised the radius to $k = 1$ and indicated the constraint on s to the surface of the sphere with

$$s_+ = \sqrt{1 - l^2} \; . \tag{15}$$

For incident light which is plane-polarised along the x axis, we can derive a vectorial strength function $\boldsymbol{a}(m,n)$, from the strength factors used in the vectorial point spread function integrals [12,17,22]

$$\boldsymbol{a}(m,n) = \begin{pmatrix} (m^2 s_+ + n^2)/l^2 \\ -mn(1-s_+)/l^2 \\ -m \end{pmatrix} \tag{16}$$

where we have converted from the spherical polar representation in Richards and Wolf to Cartesian co-ordinates.

We can now model polarisation, apodisation and aperture filtering as amplitude and phase functions over the projected pupil,

$$\boldsymbol{P}_+(m,n) = \frac{1}{s_+}\,\boldsymbol{a}(m,n)S(m,n)T(m,n) \tag{17}$$

representing forward propagation only ($\alpha \le \pi/2$), where $S(m,n)$ is the apodisation function, and $T(m,n)$ is any complex transmission filter applied across the aperture of the lens. T can also be used to model aberrations.

Microscope objectives are usually designed to obey the sine condition, giving aplanatic imaging [10], for which we write the apodisation as

$$S(m,n) = \sqrt{s_+}\ . \tag{18}$$

By applying low angle and scalar approximations, we can derive from (17) a paraxial pupil function,

$$P_+(m,n) \cong T(m,n)\ . \tag{19}$$

Returning to the PSF, we have

$$\boldsymbol{E}(\boldsymbol{x}) = -\frac{\mathrm{i}k}{2\pi}\int\int_{\Sigma} \boldsymbol{P}_+(m,n)\exp(\mathrm{i}k\boldsymbol{m}_+\cdot\boldsymbol{x})\mathrm{d}m\mathrm{d}n\ , \tag{20}$$

integrated over the projected pupil area Σ. The geometry is shown in Fig. 8. We use $\boldsymbol{m}_+ = (m,n,s_+)$ to indicate that $\boldsymbol{m}$ is constrained to the pupil sphere surface.

For a clear circular pupil of aperture half–angle α, the integration area Σ_{circ} is defined by

$$0 \le l \le \sin\alpha\ , \tag{21}$$

while for a square pupil which fits inside that circle, the limits on Σ_{sq} are

$$\begin{matrix} |m| \le \sin\alpha/\sqrt{2} \\ |n| \le \sin\alpha/\sqrt{2} \end{matrix}\ . \tag{22}$$

The transmission function T is unity for a standard widefield system with no aberrations, while for a cubic phase system (4) and (5) give

$$T_{\mathrm{c}}(m,n) = \exp[\mathrm{i}kA(m^3+n^3)]\ . \tag{23}$$

3.4 High Aperture OTF Model

A high aperture analysis of the OTF is important, because the OTF has proven to be more useful than the PSF for design and analysis of low aperture wavefront coding systems. For full investigation of the spatial frequency response of a high aperture microscope, we would normally look to the 3D OTF [7,13,19,20]. We have recently published a method for calculating the 3D OTF suitable for arbitrary pupil filters [1] which can be applied directly to find the OTF for a cubic phase plate. But since an EDF system involves recording a single image at one focal depth, a frequency analysis of the 2D PSF at that focal plane is more appropriate. This can be performed efficiently using a high NA vectorial adaptation of 2D Fourier optics [22].

This adaptation relies on the Fourier projection–slice theorem [2], which states that a slice through real space is equivalent to a projection in Fourier space:

$$f(x, y, 0) \Longleftrightarrow \int F(m, n, s)\mathrm{d}s \tag{24}$$

where $F(m, n, s)$ is the Fourier transform of $f(x, y, z)$. We have already obtained the projected pupil function $\boldsymbol{P}_+(m, n)$ in (17). Taking the 2D Fourier transform and applying (24) gives the PSF in the focal plane

$$\boldsymbol{E}(x, y, 0) \Longleftrightarrow \boldsymbol{P}_+(m, n) \; . \tag{25}$$

Since fluorescence microscopy is incoherent, we then take the intensity and 2D Fourier transform once more to obtain the OTF of that slice of the PSF

$$C(m, n) \Longleftrightarrow |\boldsymbol{E}(x, y, 0)|^2 \; . \tag{26}$$

We can implement this approach using 2D fast Fourier transforms to quickly calculate the high aperture vectorial OTF for the focal plane.

3.5 Defocused OTF and PSF

To investigate the EDF performance, we need to calculate the defocused OTF. Defocus is an axial shift z_d of the point source being imaged relative to the focal point. By the Fourier shift theorem, a translation z_d of the PSF is equivalent to a linear phase shift in the 3D pupil function,

$$\boldsymbol{E}(x, y, 0 + z_\mathrm{d}) \Longleftrightarrow \exp(\mathrm{i}ksz_\mathrm{d})\boldsymbol{Q}(m, n, s) \; . \tag{27}$$

Applying the projection-slice theorem as before gives a modified version of (25)

$$\boldsymbol{E}(x, y, z_\mathrm{d}) \Longleftrightarrow \int \exp(\mathrm{i}ksz_\mathrm{d})\boldsymbol{Q}(m, n, s)\mathrm{d}s \; . \tag{28}$$

allowing us to isolate a pupil transmission function that corresponds to a given defocus z_d,

$$T_\mathrm{d}(m, n, z_\mathrm{d}) = \exp(\mathrm{i}ks_+z_\mathrm{d}) \; , \tag{29}$$

Table1. Optical parameters used for PSF and OTF simulations

Optical parameter	Simulation value
Wavelength	530 nm
Numerical aperture	NA = 1.3 oil
Oil refractive index	$n_1 = 1.518$
Aperture half angle	$\alpha = \pi/3$
Pupil shape	Square
Pupil width	7.1 mm
Cubic phase strength	25.8 waves peak to valley

which we incorporate into the projected pupil function $\boldsymbol{P}_+(m,n)$ from (17), giving

$$\boldsymbol{P}_+(m,n,z_\mathrm{d}) = \frac{1}{s_+}\,\boldsymbol{a}(m,n)S(m,n)T_\mathrm{d}(m,n,z_\mathrm{d})T_\mathrm{c}(m,n)\ . \tag{30}$$

If we assume a low aperture pupil, we can approximate (15) to second order, giving the well known paraxial aberration function for defocus

$$T_\mathrm{d}(m,n,z_\mathrm{d}) \cong \exp\left(-\mathrm{i}kz_\mathrm{d}\frac{l^2}{2}\right)\ . \tag{31}$$

Finally, using $\mathcal{F}$ to denote a Fourier transform, we write down the full algorithm for calculating the OTF of a transverse slice through the PSF:

$$C(m,n,z_\mathrm{d}) = \mathcal{F}^{-1}\left\{\left|\mathcal{F}\left[\boldsymbol{P}_+(m,n,z_\mathrm{d})\right]\right|^2\right\}\ . \tag{32}$$

It is convenient to calculate the defocused PSF using the first step of the same approach:

$$\boldsymbol{E}(x,y,z_\mathrm{d}) = \mathcal{F}\left[\boldsymbol{P}_+(m,n,z_\mathrm{d})\right]\ . \tag{33}$$

3.6 Simulation Results

We have applied this theoretical model to simulate the wavefront coding experiments described earlier, using the parameters given in Table 1. The theoretical assumption that the incident light is plane polarised corresponds to the placement of an analyser in the microscope beam path. This polarisation explains some *xy* asymmetry in the simulation results.

Due to the large phase variation across the pupil, together with the large defocus distances under investigation, a large number of samples of the cubic phase function were required to ensure accuracy and prevent aliasing. We created a 2D array with 1024^2 samples of the pupil function $\boldsymbol{P}+$ from (30) using (22) for the aperture cutoff. We then padded this array out to 4096^2 to allow for sufficient sampling of the resulting PSF, before employing the algorithms in (33) and (32) to calculate the PSF and OTF respectively. Using fast Fourier transforms, each execution of (32) took about 8 minutes on a Linux Athlon 1.4 GHz computer with 1 GB of RAM.

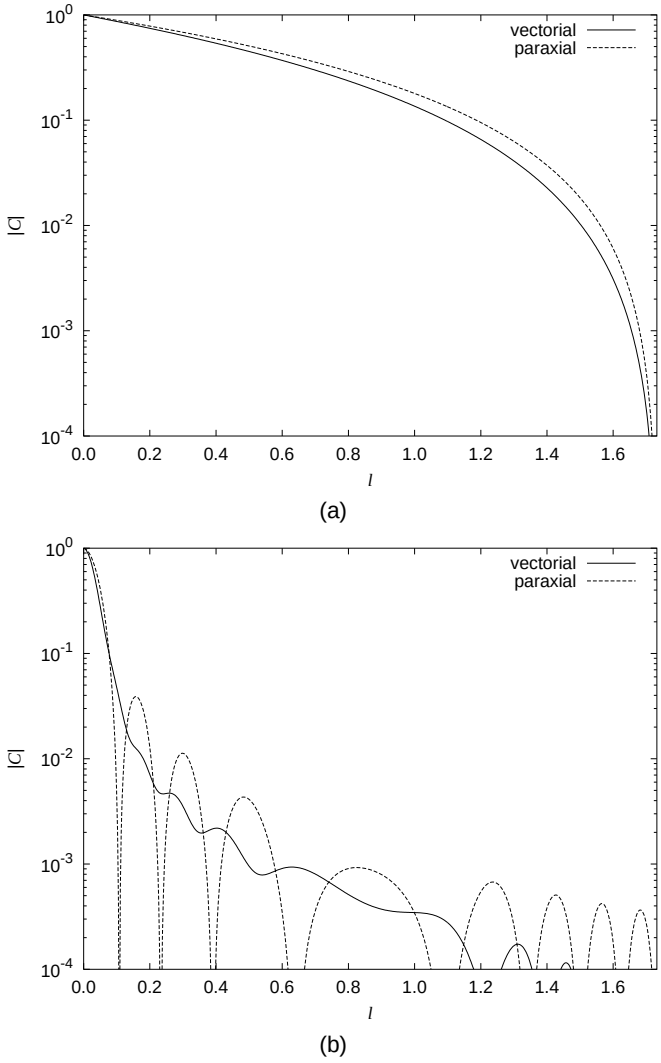

Figure9. A comparison of widefield (no CPM) OTFs using our vectorial (*solid line*) and paraxial (*dashed line*) simulations: (**a**) in–focus at $z_d = 0\,\mu m$ and (**b**) defocused to $z_d = 4\,\mu m$. For a diagonal line through the OTF along $m = n$, we have plotted the value of the 2D projected OTF for each case. While the structure of the in–focus OTF curves is similar for the two models, the relative difference between them increases with spatial frequency, reaching over 130% at the cutoff. Once defocus is applied, the two models predict markedly different frequency response in both structure and amplitude

The wavefront coding inverse filter for our experiments was derived from the theoretical widefield (no CPM) OTF and the measured CPM OTF. The discrepancy in the focal plane theoretical widefield OTF between the paraxial approximation

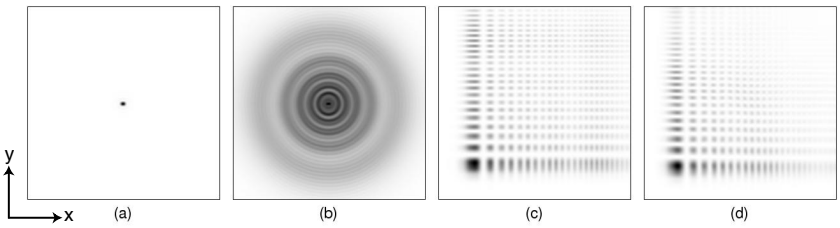

Figure10. The simulated vectorial high aperture PSF for widefield and wavefront coding, showing the effect of defocus: (**a**) widefield in–focus $z_d = 0\,\mu$m, (**b**) widefield defocused $z_d = 4\,\mu$m, (**c**) CPM in–focus $z_d = 0\,\mu$m, (**d**) CPM defocused $z_d = 4\,\mu$m. This amount of defocus introduces very little discernible difference between the CPM PSFs. Indeed paraxial CPM simulations (not shown here) are also similar in structure. The PSFs shown have the same area as Fig. 5 (13 µm×13 µm). The incident polarisation is in the *x* direction. The images are normalised to the peak intensity of each case. Naturally the peak intensity decreases with defocus, but much less rapidly in the CPM system

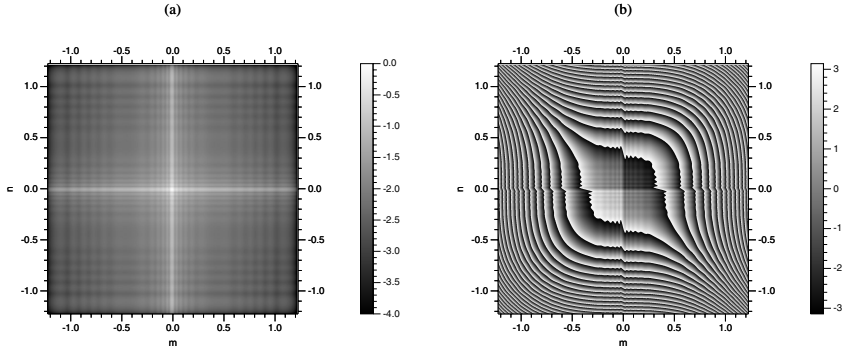

Figure11. The simulated vectorial high aperture in–focus CPM OTF: (**a**) is the magnitude of the OTF in $\log_{10}$ scale, and (**b**) is the wrapped phase in radians. While the frequency response is much stronger along the *m* and *n* axes, the magnitude remains above 10^{-3} throughout the spatial frequency cutoff. The phase of the OTF is very similar to the cubic phase in the pupil. Compensating for the OTF phase is important in digital restoration. The $z_d = 4\,\mu$m defocused OTF (not shown) has a similar appearance to this in–focus case. See Fig. 6 to compare with the measured OTFs

and our vectorial high aperture calculation is shown in Fig. 9(a). We show a similar comparison of the defocused widefield OTF in Fig. 9(b). We can see there is a major difference in the predictions of the two models, especially at high frequencies. The discrepancy between the models increases markedly with defocus. This implies that the best deconvolution accuracy will be obtained by using the vectorial widefield OTF when constructing the digital inverse filter for a high aperture system.

We now investigate the simulated behaviour of a CPM system according to our vectorial theory. Figures 10 and 11 show the vectorial high aperture PSF and OTF for the focal plane with a strong CPM. The defocused $z_d = 4\,\mu$m vectorial CPM

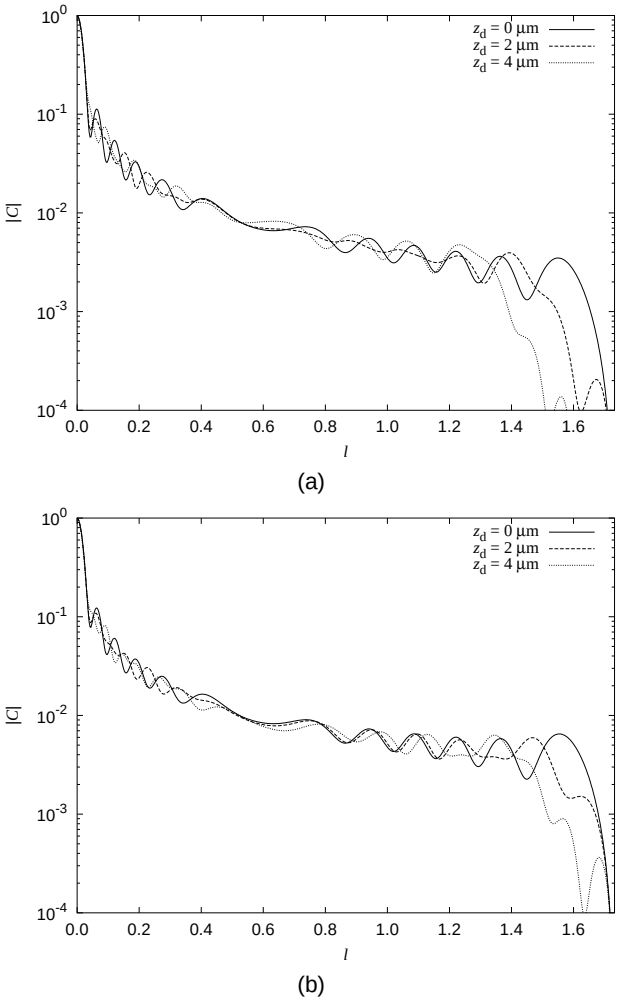

Figure12. The magnitude of the wavefront coding OTF for the (**a**) vectorial and (**b**) paraxial models, plotted along a diagonal line $m = n$ through the OTF, with different values of defocus: in–focus $z_d = 0\,\mu$m (*solid line*), defocused $z_d = 2\,\mu$m (*dashed line*), defocused $z_d = 4\,\mu$m (*dotted line*). In common with the the widefield system, the models differ the most at high spatial frequencies, up to 300% for the in–focus case. As defocus increases, the differences become more extreme, with the vectorial simulation predicting a quicker reduction in effective cutoff

OTF (not shown) and the paraxial in–focus and defocused $z_d = 4\,\mu$m CPM PSFs and OTFs (not shown) are all qualitatively similar to the vectorial CPM results shown in Figs. 10 and 11.

However, if we perform a quantitative comparison we see that there are marked differences. Figure 12 shows the relative strength of the CPM OTF for a diagonal

cross section. The differences between the models are similar to the widefield OTF in Fig. 9(a) for the in–focus case, with up to 100% difference at high spatial frequencies. However, as the defocus increases, the structure of the vectorial CPM OTF begins to diverge from the paraxial model, as well as the point where the strength drops below 10^{-4}. This is still a much lower discrepancy than the widefield model for similar amounts of defocus, as is clear by comparison with Fig. 9.

These plots allow us to assess the SNR requirements for recording images with maximum spatial frequency response. For both widefield and CPM systems, the experimental dynamic range will place an upper limit on the spatial frequency response. In widefield a 10^3 SNR of will capture nearly all spatial frequencies up to the cutoff (see Fig. 9(a)), allowing for good contrast throughout. Further increases in SNR will bring rapidly diminishing returns, only gradually increasing the maximum spatial frequency response.

For CPM imaging the same 10^3 SNR will produce good contrast only for low spatial frequencies, with the middle frequencies lying less than a factor of ten above the noise floor, and the upper frequencies dipping below it. However, a SNR of 10^4 will allow a more reasonable contrast level across the entire OTF. For this reason, a 16 bit camera, together with other noise control measures, is needed for a CPM system to achieve the full resolution potential of high aperture lenses. This need for high dynamic range creates a trade off for rapid imaging of living specimens – faster exposure times will reduce the SNR and lower the resolution.

Arguably the most important OTF characteristic used in the EDF digital deconvolution is the phase. As can be seen from Fig. 11 the CPM OTF phase oscillates heavily due to the strong cubic phase. This corresponds to the numerous contrast reversals in the PSF. The restoration filter is derived from the OTF, and therefore accurate phase in the OTF is needed to ensure that any contrast reversals are correctly restored.

A comparison of the amount of OTF phase difference between focal planes for the vectorial and paraxial models is shown in Fig.13. We calculated this using the unwrapped phase, obtained by taking samples of the OTF phase along a line $m = n$, then applying a 1D phase unwrapping algorithm to those samples. After finding the unwrapped phases for different focal planes, $z_\mathrm{d} = 2\,\mu\mathrm{m}$ and $z_\mathrm{d} = 4\,\mu\mathrm{m}$, we then subtracted them from the in focus case at $z_\mathrm{d} = 0\,\mu\mathrm{m}$.

Ideally the OTF phase difference between planes within the EDF range should be very small. It is clear however that there are some notable changes with defocus. Both paraxial and vectorial models show a linear phase ramp, with oscillations.

This linear phase ramp is predicted by the stationary phase approximation to the 1D CPM OTF, Eq. (A12) in Dowski and Cathey [6]. Since the Fourier transform of a phase ramp is a lateral displacement, this gives a lateral motion of the PSF for different focal planes. In practice this has the effect of giving a slightly warped projection. A mismatch between the microscope OTF and the inverse filter of this sort will simply result in a corresponding offset of image features from that focal plane. Otherwise spatial frequencies should be recovered normally.

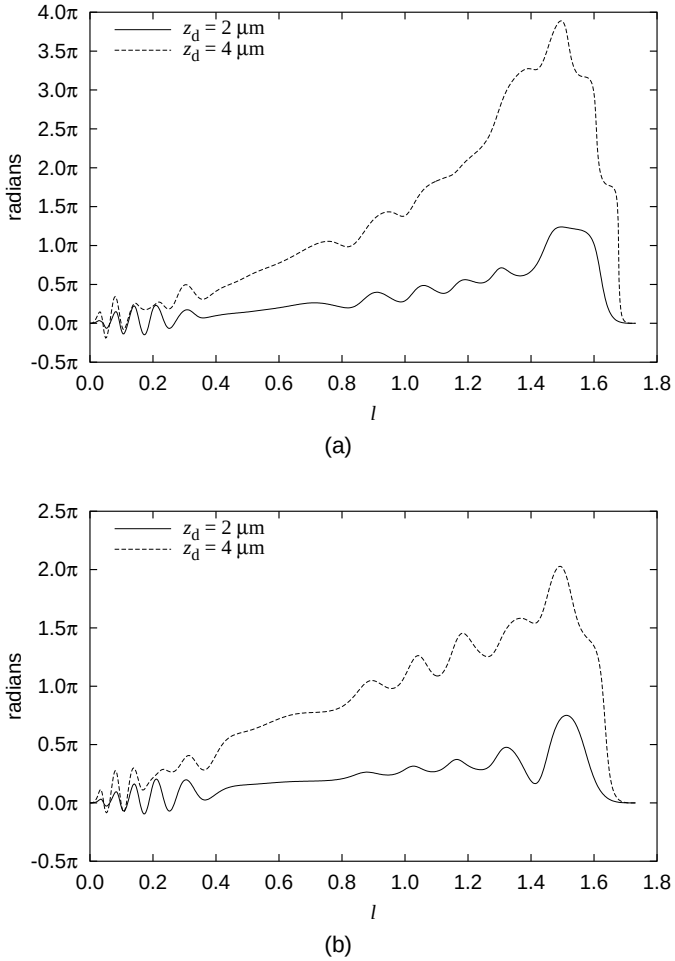

Figure13. The relative OTF phase angle between focal planes, along a diagonal line $m = n$ through the CPM OTF, for (**a**) the vectorial model, and (**b**) the paraxial model. For both (a) and (b) we show two cases, the unwrapped phase difference between the $z_d = 0\,\mu$m and $z_d = 2\,\mu$m OTF (*solid line*) and the unwrapped phase difference between $z_d = 0\,\mu$m and $z_d = 4\,\mu$m (*dashed line*). All cases show a linear phase ramp with an oscillation of up to $\pi/2$. This phase ramp corresponds to a lateral shift of the PSF. The vectorial case shows an additional curvature and larger overall phase differences of up to 4π radians (or 2 waves) across the spectrum

The oscillations will have a small effect; they are rapid and not overly large in amplitude: peaking at $\pi/2$ for both vectorial and paraxial models. This will effectively introduce a source of noise between the object and the final recovered image.

Whilst these oscillations are not predicted by the stationary phase approximation, they are still evident for the paraxial model.

The most dramatic difference between the two models is in the curvature of the vectorial case, which is particularly striking in the $z_d = 4\,\mu m$ plane, and not discernible at all in the paraxial case (Fig.13). This primary effect of this curvature will be to introduce some additional blurring of specimen features in the $z_d = 4\,\mu m$ plane, which the inverse filter will not be able to correct. The total strength of this curvature at $z_d = 4\,\mu m$ is about 2π across the complete $m = n$ line, or one wave, which is a significant aberration.

3.7 Discussion

The CPM acts as a strong aberration which appears to dominate both the effects of defocus and of vectorial high aperture focusing. The paraxial approximation certainly loses accuracy for larger values of defocus, but not nearly so much as in the defocused widefield case. Yet significant differences remain between the two models, notably a one wave curvature aberration in the vectorial case, and this suggests that vectorial high aperture theory will be important in the future design of high aperture wavefront coding systems.

We can also look at the two models as providing an indication of the difference in performance of CPM wavefront coding between low aperture and high aperture systems. The curvature aberration in the high aperture case varies with defocus, which means that it cannot be incorporated into any 2D digital deconvolution scheme. This effectively introduces an additional blurring of specimen features in planes away from focus, lowering the depth of field boost achieved with the same CPM strength in a low aperture wavefront coding system.

In general the CPM performs a little better at low apertures for EDF applications. But the high aperture CPM system still maintains useful frequency response across the full range of an equivalent widefield system, especially for on–axis frequencies.

4 Conclusion

Wavefront coding is a new approach to microscopy. Instead of avoiding aberrations, we deliberately create and exploit them. The aperture of the imaging lens still places fundamental limits on performance. However wavefront coding allows us to trade off those limits between the different parameters we need for a given imaging task. Focal range, signal to noise, mechanical focus scanning speed and maximum frequency response are all negotiable using this digital–optical approach to microscopy.

The high aperture experimental results presented here point to the significant promise of wavefront coding. The theoretical simulations predict an altered behaviour for high apertures, which will become more important with higher SNR imaging systems. For large values of defocus, these results predict a tighter limit

on the focal range of EDF imaging than is the case for paraxial systems, as well as additional potential for image artefacts due to aberrations.

The fundamental EDF behaviour remains in force at high apertures, as demonstrated by both experiment and theory. This gives a solid foundation to build on. The CPM was part of the first generation wavefront coding design. Using simulations, new phase mask designs can be tested for performance at high apertures before fabrication. With this knowledge, further development of wavefront coding techniques may be carried out, enhancing its use at high apertures.

Acknowledgments

We would like to thank W. Thomas Cathey and Edward R. Dowski Jr. of CDM Optics Inc, Boulder, CO, USA. Experimental assistance was provided by Elanor Kable, Theresa Dibbayawan, David Philp and Janey Lin at the University of Sydney and Claude Rosignol at Colorado University.

References

1. Matthew R. Arnison and Colin J. R. Sheppard. A 3D vectorial optical transfer function suitable for arbitrary pupil functions. *Opt. Commun.*, 211(1-6):45–55, 2002.
2. R. N. Bracewell. *Two-dimensional imaging*. Prentice Hall, Englewood Cliffs, NJ, USA, 1995.
3. Sara Bradburn, W. Thomas Cathey, and Edward R. Dowski, Jr. Realizations of focus invariance in optical-digital systems with wave-front coding. *App. Opt.*, 36(35):9157–9166, 1997.
4. Juan Campos, Juan C. Escalera, Colin J. R. Sheppard, and María J. Yzuel. Axially invariant pupil filters. *J. Mod. Optics*, 47(1):57–68, 2000.
5. Wanli Chi and Nicholas George. Electronic imaging using a logarithmic asphere. *Opt. Lett.*, 26(12):875–877, 2001.
6. Edward R. Dowski, Jr. and W. Thomas Cathey. Extended depth of field through wave-front coding. *App. Opt.*, 34(11):1859–1866, 10 April 1995.
7. B. R. Frieden. Optical transfer of the three-dimensional object. *J. Opt. Soc. Am.*, 57:56–66, 1967.
8. G. Häusler. A method to increase the depth of focus by two step image processing. *Opt. Commun.*, 6(1):38–42, 1972.
9. P. D. Higdon, Peter Török, and Tony Wilson. Imaging properties of high aperture multi-photon fluorescence scanning optical microscopes. *J. Microsc.*, 193(2):127–141, February 1999.
10. H. H. Hopkins. The Airy disc formula for systems of high relative aperture. *Proc. Phys. Soc.*, 55:116, 1943.
11. R. Juškaitis, M. A. A. Neil, F. Massoumian, and T. Wilson. Strategies for wide-field extended focus microscopy. In *Focus on microscopy*, Amsterdam, April 2001.
12. M Mansuripur. Distribution of light at and near the focus of high-numerical-aperture objectives. *J. Opt. Soc. Am. A*, 3(12):2086–2093, 1986.
13. C W McCutchen. Generalized aperture and the three-dimensional diffraction image. *J. Opt. Soc. Am.*, 54:240–244, 1964.

14. Jorge Ojeda-Castañeda, R. Ramos, and A. Noyola-Isgleas. High focal depth by apodization and digital restoration. *Appl. Opt.*, 27:2583–2586, 1988.
15. Jorge Ojeda-Castañeda, E. Tepichin, and A. Diaz. Arbitrarily high focal depth with a quasioptimum real and positive transmittance apodizer. *Appl. Opt.*, 28(13):2666–2670, 1989.
16. P. Potuluri, Matthew Fetterman, and David Brady. High depth of field microscopic imaging using an interferometric camera. *Opt. Express*, 8(11):624, May 2001.
17. B. Richards and E. Wolf. Electromagnetic diffraction in optical systems II. Structure of the image field in aplanatic systems. *Proc. Roy. Soc. A*, 253:358–379, 1959.
18. C. J. R. Sheppard. Depth of field in optical microscopy. *J. Microsc.*, 149:73–75, 1988.
19. C. J. R. Sheppard and C. J. Cogswell. *Confocal microscopy*, chapter Three-dimensional imaging in confocal microscopy, pages 143–169. Academic Press, London, 1990.
20. C J R Sheppard, M Gu, Y Kawata, and S Kawata. Three-dimensional transfer functions for high aperture systems obeying the sine condition. *J. Opt. Soc. Am. A*, 11:593–598, 1994.
21. C. J. R. Sheppard, D. K. Hamilton, and I. J. Cox. Optical microscopy with extended depth of field. *Proc. R. Soc. Lond. A*, A387:171–186, 1983.
22. C. J. R. Sheppard and K. G. Larkin. Vectorial pupil functions and vectorial transfer functions. *Optik*, 107(2):79–87, 1997.
23. P. Török, P. Varga, Z. Laczik, and G. R. Booker. Electromagnetic diffraction of light focussed through a planar interface between materials of mismatched refractive indices: an integral representation. *J. Opt. Soc. Am. A*, 12(2):325–332, 1995.
24. Sara C. Tucker, W. Thomas Cathey, and Edward R. Dowski, Jr. Extended depth of field and aberration control for inexpensive digital microscope systems. *Optics Express*, 4(11):467–474, 1999.
25. W T Welford. Use of annular apertures to increase focal depth. *J. Opt. Soc. Am.*, 50(8):749–753, 1960.
26. T. Wilson, MAA. Neil, and F. Massoumian. Point spread functions with extended depth of focus. In *Proc. SPIE*, volume 4621, pages 28–31, San Jose, CA, USA, January 2002.